Supporting Information for

Electrocatalytic Nitrogen Reduction to Ammonia by Graphene-Supported Au_4Cu_2 and Au_2Ag_2 Nanoclusters

Aamir Shehzad,[ab] Qiuhao Yi,[a] Chaonan Cui,[a] Zhixun Luo*[ab]

State Key Laboratory for Structural Chemistry of Unstable and Stable Species, Institute of Chemistry, Chinese Academy of Sciences, Beijing 100190, China; School of Chemistry, University of Chinese Academy of Sciences, Beijing 100049, China.

* Corresponding author. Email: zxluo@iccas.ac.cn (ZL).

S1. Materials and Methods

Materials. The chemicals and reagents utilized for the synthesis of these clusters comprise silver nitrate ($AgNO_3$, 99.999%, Alfer Aeser), cupric acetate [$Cu(OAC)_2$, 99.999%, Alfer Aeser], phenylacetylene (PA, C_8H_6, 98%, Innochem), sodium borohydride ($NaBH_4$, ≥98.0%, Sigma Aldrich), chloro(triphenylphosphine)gold(I) (PPh_3)AuCl (99%, Innochem), dichloromethane (CH_2Cl_2), and absolute ethanol (C_2H_5OH, ≥99.8%, Sigma-Aldrich). All experiments employed ultrapure H_2O. All chemicals were procured from commercial sources and used as received. Various chemicals, including graphene, KOH, NaOH, HCl, salicylic acid, sodium citrate, sodium hypochlorite (NaClO), sodium nitroferricyanide dihydrate ($C_5FeN_6Na_2O.2H_2O$), NH_4Cl, p-dimethylaminobenzaldehyde ($C_9H_{11}NO$), hydrazine monohydrate ($N_2H_4.H_2O$), and Nafion D521 (5 wt%), were acquired commercially and used without additional purification. The water utilized for the experiment was Milli-Q water, generated by a Millipore system. Carbon paper electrode was used for the ENRR experiments.

Quantification of hydrazine byproduct. During the reduction of N_2 to NH_3, hydrazine (N_2H_2) serves as a competitive by-product. The quantity of hydrazine was spectrophotometrically measured by the Watt and Chrisp method.[1] Under acidic circumstances, hydrazine reacts with p-dimethylaminobenzaldehyde ($C_9H_{11}NO$) to yield yellow molecules that demonstrate UV-vis absorbance at 455 nm, enabling the spectrophotometric detection of N_2H_2. This study employed a color reagent solution comprising 30 mL of HCl, 300 mL of ethanol, and 5.99 g of p-

dimethylaminobenzaldehyde. The standard reference solutions were prepared with $N_2H_4.H_2O$ (85%) at concentrations of 0, 0.1, 0.2, 0.3, 0.4, 0.5, and 0.6 $\mu g.mL^{-1}$ to establish the calibration curve. To ascertain hydrazine levels, 5 mL of the color reagent and 5 mL of each reference solution were included in the ENRR solution for analysis. After a 15-minute incubation period, absorbance was assessed at 457 nm. The UV-vis absorption data for N_2H_4 standard solutions produced a calibration curve described by the equation y=1.290x–0.00379 (R^2=0.999), demonstrating a robust linear relationship between absorbance values and hydrazine concentrations (Fig. S2). The hydrazine yield for each ENRR experiment was assessed by combining 5 mL of the color reagent with 5 mL of the residual electrolyte, followed by the acquisition of UV-vis absorption spectra after a 15-minute incubation period.

Instrumentation. The UV-visible absorption spectra were obtained utilizing a Shimadzu UV-3600 UV-vis-NIR spectrophotometer. The single-crystal X-ray diffraction (SC-XRD) results were obtained using a Rigaku MM007HF Saturm724+ single-crystal X-ray diffractometer with Mo Kα radiation (λ=0.71073 Å). The single crystal structure was elucidated using direct techniques and refined by full-matrix least-squares on F^2. The infrared (IR) analysis was performed utilizing the VETEX 70v. X-ray photoelectron spectroscopy (XPS) was conducted using a Thermo Fisher Scientific EscaLab250Xi spectrometer to elucidate the surface atoms in the single crystal structure, based on crystal structure data and core-level binding energies (BEs) relative to their surface oxidation states. The high-resolution morphological characteristics of graphene-supported nanoclusters were analysed using a high-resolution transmission electron microscope (HRTEM) JSM200FS.

Computational Method. The DFT-calculated energy diagrams and TD-DFT calculations were performed using the Gaussian 16 program,[2] employing the LANL2TZ basis set for metal atoms (Au, Ag, and Cu) and the STO-3G basis set for nonmetal atoms (H, C, and P). The PBE0 hybrid functional was utilized to model the electronic structure and absorption spectrum of several ligand-protected metal clusters by incorporating 10-100 potential transitions. Multiwfn software was used to plot the charge transfer spectra to intuitively analyze the intrinsic characteristics of the electronic excitation and the subsequent redistribution.

S2. Experimental Details

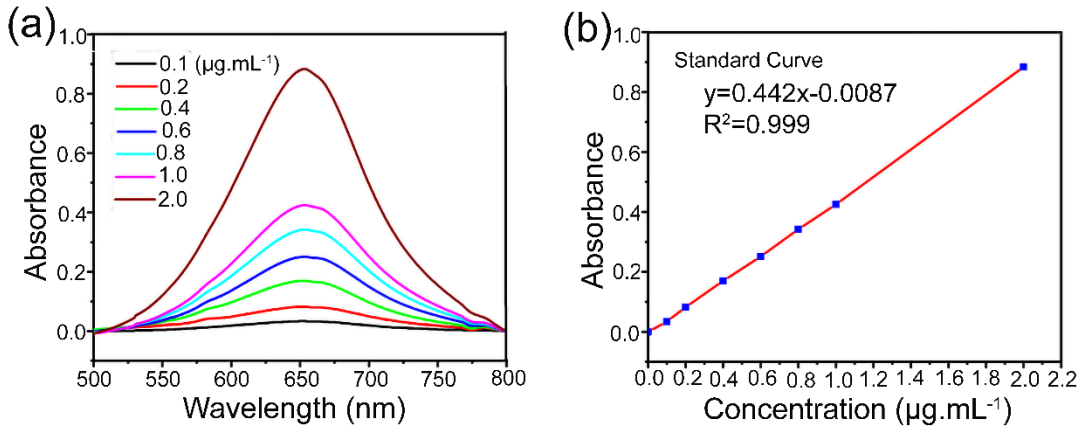

Fig. S1 (a) UV-vis absorption spectra of indophenol assays with NH_4^+ ions after incubation for 2 hours at room temperature in dark conditions. **(b)** Calibration curve used for determination of NH_3 concentration.

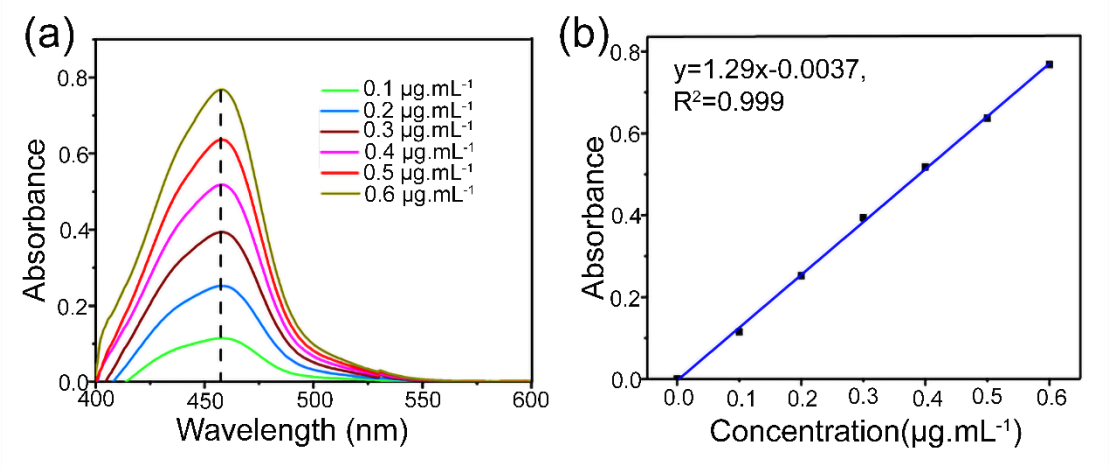

Fig. S2 (a) UV-vis absorption spectra for N_2H_4 standard solutions with different concentrations. **(b)** Calibration curve used for estimation of N_2H_4 concentration.

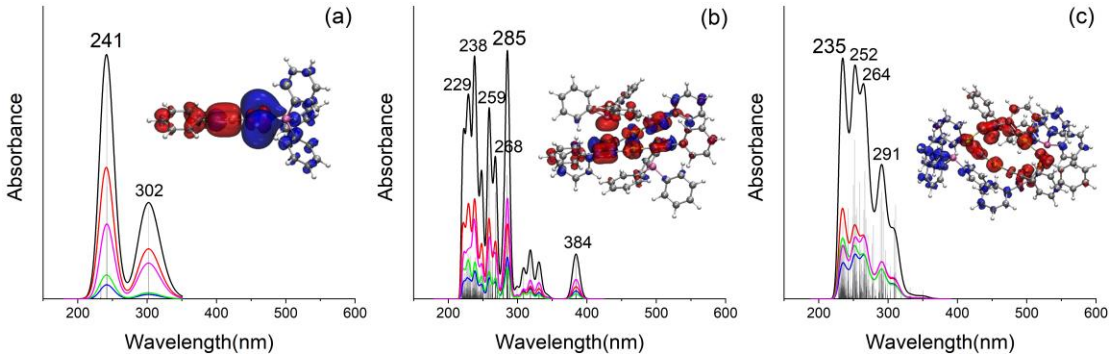

Fig. S3 Hole-electron analysis and TDDFT-calculated charge-transfer spectra of different ligand-protected metal clusters featuring **(a)** single Au atom, **(b)** Au_2Ag_2 and **(c)** Au_4Cu_2 as the centre, respectively. The lines in black, red, blue, green and purple represent the total spectrum, redistribution of ligand, redistribution of metal, electron transfer from metal to ligand, and electron transfer from ligand to metal, respectively. The insets display the hole (red)-electron (blue) distribution of the corresponding excited state for the dominant peak in the UV-vis absorption spectrum.

We conducted the hole-electron analysis to depict the excitation process corresponding to the UV-vis absorption peaks of the $Au_2Ag_2(PPh_3)_2(PhC{\equiv}C)_4$, $Au_4Cu_2(PPh_3)_4(PhC{\equiv}C)_6$ and $Au(PPh_3)(PhC{\equiv}C)$ clusters. As we can see in the insets of Fig. S3a, the hole distribution locates on the phenylacetylene ligand, while the electron distribution mainly locates on Au atom and triphenylphosphine ligand, suggesting that the excitation of electrons is from the electron-rich phenylacetylene ligand to triphenylphosphine ligand and Au metal atom, which is consistent with previous results of charge transfer spectrum. For $Au_2Ag_2(PPh_3)_2(PhC{\equiv}C)_4$ crystal (Fig. S3b), the portion of charge transfer from ligand to metal grows, which could be explained by the enhanced ligand-metal interaction through the coordination between added Ag atom and C atom in triphenylphosphine ligand. For $Au_4Cu_2(PPh_3)_4(PhC{\equiv}C)_6$ crystal (Fig. S3c), the portion of charge transfer from metal to ligand also grows, and the excitation of electrons is from phenylacetylene ligand and Cu atom to phenylacetylene ligand accordingly. The reversed charge transfer might come from the reduced electronegativity of the Cu atom compared to Au and Ag atoms. In general, dppy ligand tends to donate electrons and remain holes in the excitation process, while the phenylacetylene ligand serves as an electron acceptor. The centre metal atom or clusters could either donate or accept electrons, which depends on their intrinsic electronegativity and structure. So, the adjustment of different coordination numbers of ligands and the kind of metal centre in these metal clusters refines the shape and peak position of their UV-vis absorption spectrum.

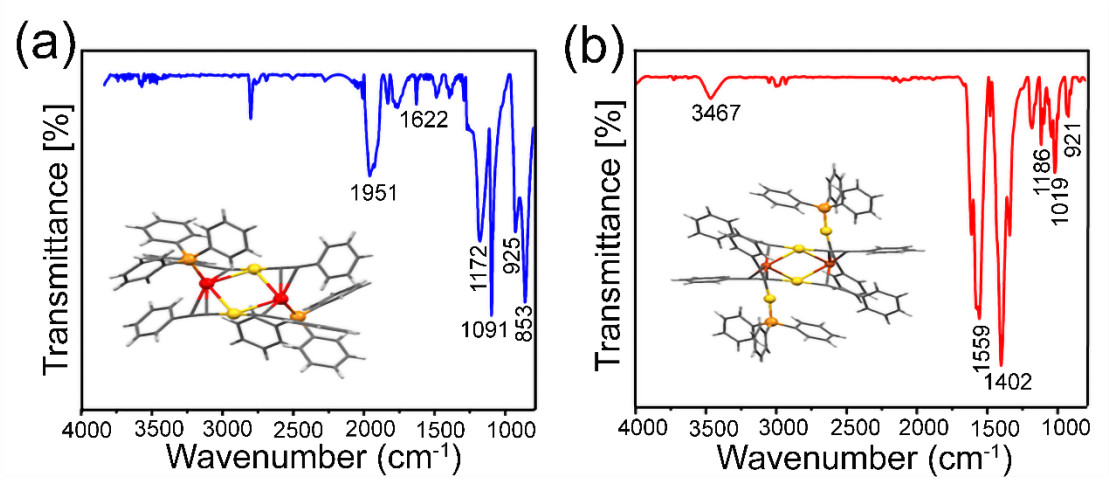

Fig. S4 IR spectra of the $Au_2Ag_2(PPh_3)_2(PhC{\equiv}C)_4$ **(a)** and $Au_4Cu_2(PPh_3)_4(PhC{\equiv}C)_6$ **(b)** nanoclusters.

The IR spectra reveal that the sharp peak at 853 cm^{-1} corresponds to the out-of-plane C–H bending vibrations of phenyl rings or may represent P–C stretching vibrations. A medium signal at 925 cm^{-1} is attributed to C–H bending vibrations associated with the asymmetrical bending of the phenyl-acetylene ligands in the produced cluster. The notable peak at 1091 cm^{-1} is likely linked to the C–C stretching of the phenyl-acetylene ligand. A medium peak at 1172 cm^{-1} signifies C–C stretching in aromatic compounds, showing the presence of phenyl rings in the synthesized clusters. The notable peak at 1951 cm^{-1} likely indicates C≡C stretching vibrations, characteristic of alkynes, suggesting the presence of the phenyl-acetylene ligand. A slight peak at 1622 cm^{-1} may suggest C=C stretching vibrations of such conjugated systems with the phenyl groups.

Fig. S4b shows the IR-spectra of the Au_4Cu_2 NCs. According to the IR spectrum, the weak peaks at 921 cm^{-1}, 1019 cm^{-1}, and 1186 cm^{-1} are characteristic of C–H bending vibrations in aromatic rings, suggesting that the phenyl group is intact. The weak signal at 1334 cm^{-1} and strong peak at 1402 cm^{-1} are likely due to C–C and C=C stretching in aromatic systems. The broad peak at 1559 cm^{-1} further supports the presence of aromatic C=C stretching. The weak peaks at 2931 cm^{-1} and 3467 cm^{-1} suggest minor aliphatic C–H and O–H stretching, possibly due to solvent residues/moisture.

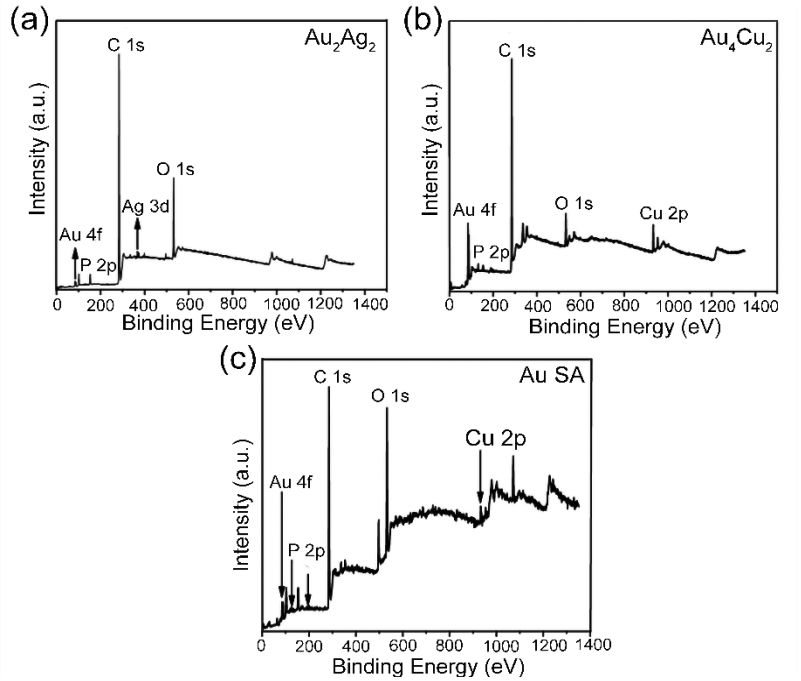

Fig. S5 XPS survey spectra of **(a)** Au_2Ag_2 NCs and **(b)** Au_4Cu_2 NCs, in comparison with that of the Au complex **(c)**.

The XPS survey spectra of the Au complex, Au_2Ag_2 and Au_4Cu_2 NCs are presented in Fig. S5, demonstrating the alignment of data with SC-XRD results.

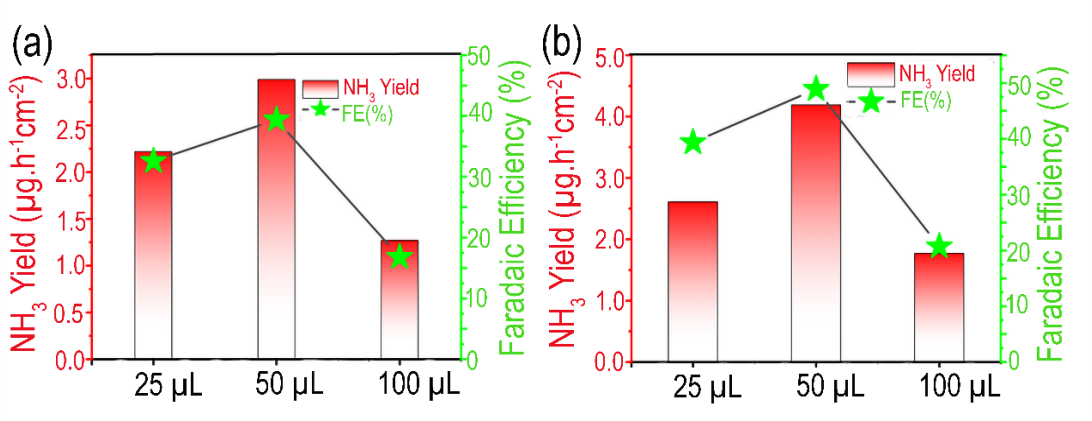

Fig. S6 Comparison of ENRR performance using graphene-supported **Au_4Cu_2** NCs with **(a)** 25 mg and **(b)** 50 mg of graphene amounts and varying loading volumes (25 µL, 50 µL, and 100 µL) at -0.8 V vs. RHE.

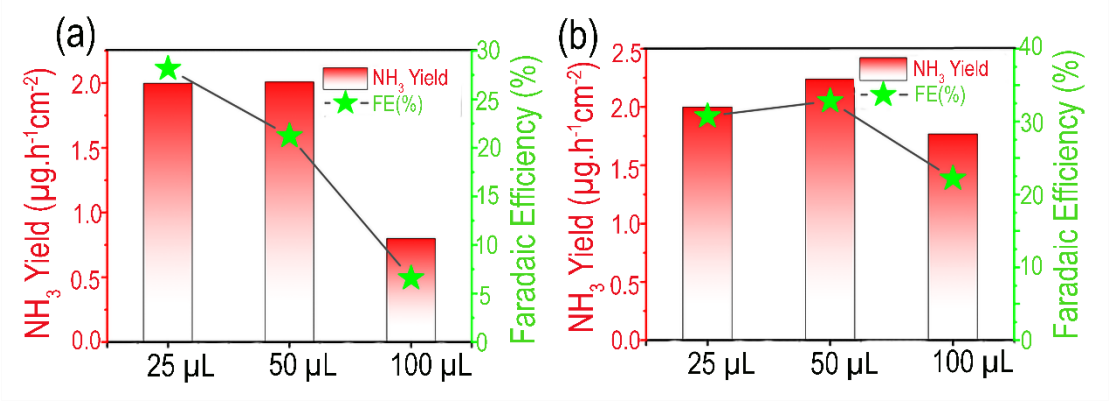

Fig. S7 Comparison of ENRR performance using graphene-supported **Au_2Ag_2** NCs with **(a)** 25 mg **(b)** 50 mg of graphene amounts and varying loading volumes (25 µL, 50 µL, and 100 µL) at -0.8 V vs. RHE.

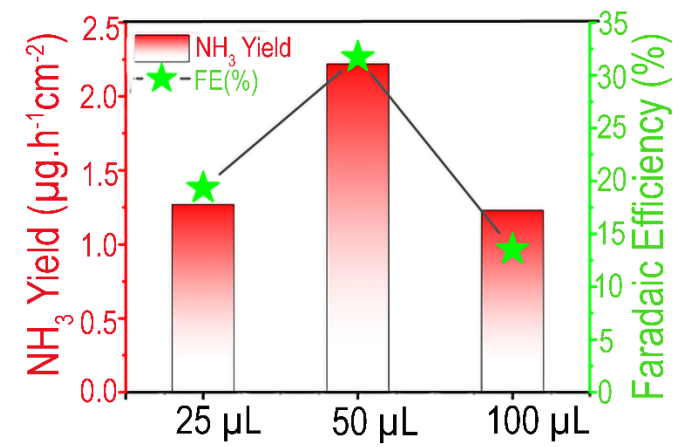

Fig. S8 Comparison of ENRR performance using 50 mg of graphene-supported Au(PPh_3)(PhC≡C) with varying loading volumes (25 µL, 50 µL, and 100 µL) at -0.8 V vs. RHE.

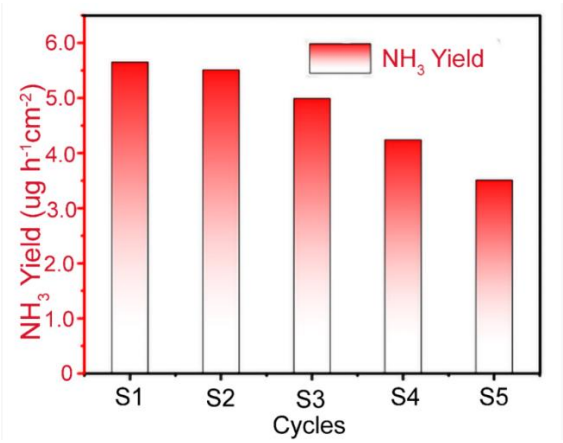

Fig. S9 NH_3 yield using graphene-supported Au_4Cu_2 NCs at -0.8 V vs. RHE during recycling test 5 times.

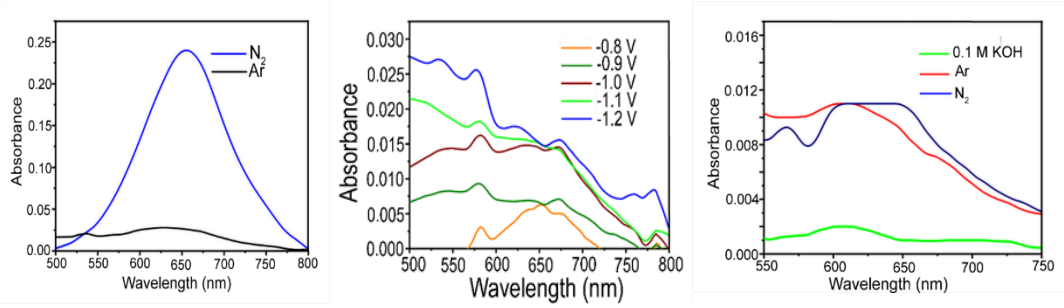

Fig. S10 (Left) NRR test in two different environments (N_2 or Ar) to confirm the source of ammonia using 0.1 M KOH as the electrolyte at -0.8 V vs. RHE. **(Middle)** Exclusion NRR tests in Ar-saturated environment using 0.1 M KOH as the electrolyte at potentials ranging from -1.2 V to -0.8 V vs. RHE. **(Right)** Exclusion NRR test without catalyst in different environments.

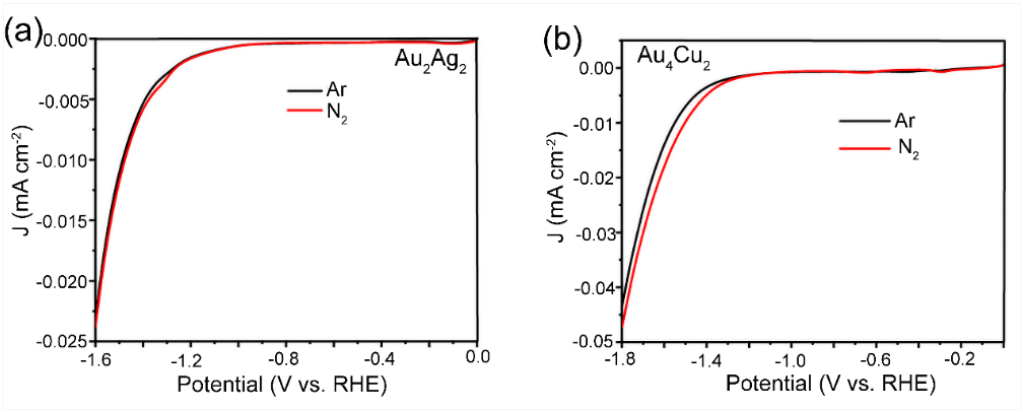

Fig. S11 A comparison of NRR activity confirmation by unsupported **(a)** Au_2Ag_2 and **(b)**Au_4Cu_2 nanoclusters.

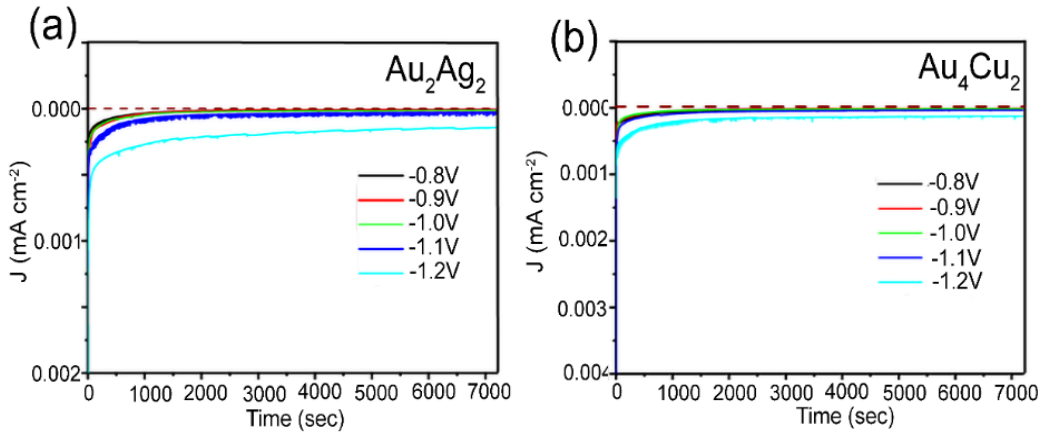

Fig. S12 A comparison of chronoamperometry curves at corresponding potentials using unsupported **(a)** Au_2Ag_2 and **(b)** Au_4Cu_2 nanoclusters.

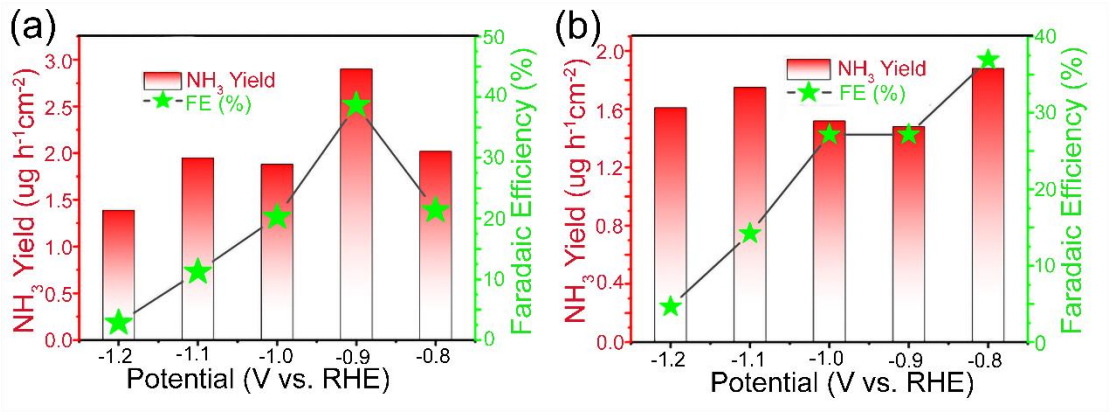

Fig. S13 A comparison of ammonia yield rate and Faradaic efficiencies for unsupported **(a)** Au_4Cu_2 **(a)** and **(b)** Au_2Ag_2 nanoclusters at varying potentials.

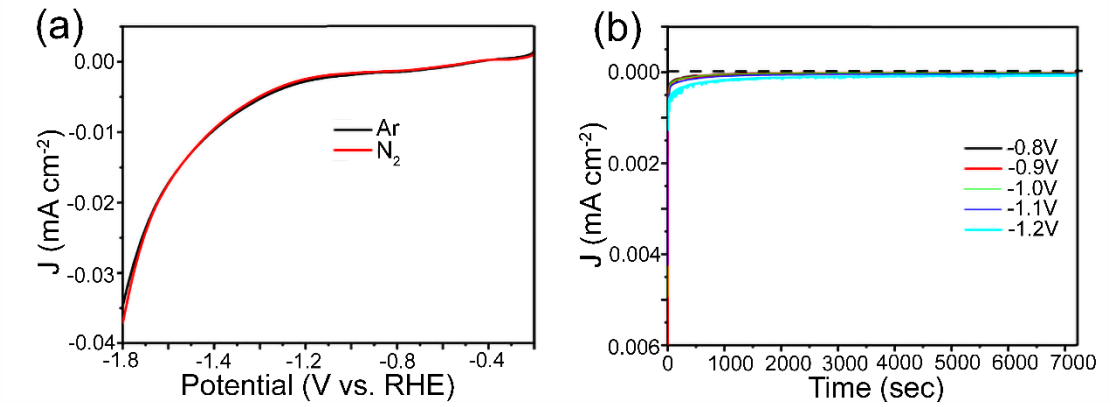

Fig. S14 A comparison of LSV curves for Au_2Ag_2 NCs on graphene in N_2 and Ar-saturated 0.1 M KOH electrolyte solution **(a)**, and the time-dependent current density curves for Au_2Ag_2 on graphene at various potentials in 0.1 M KOH solution **(b)**.

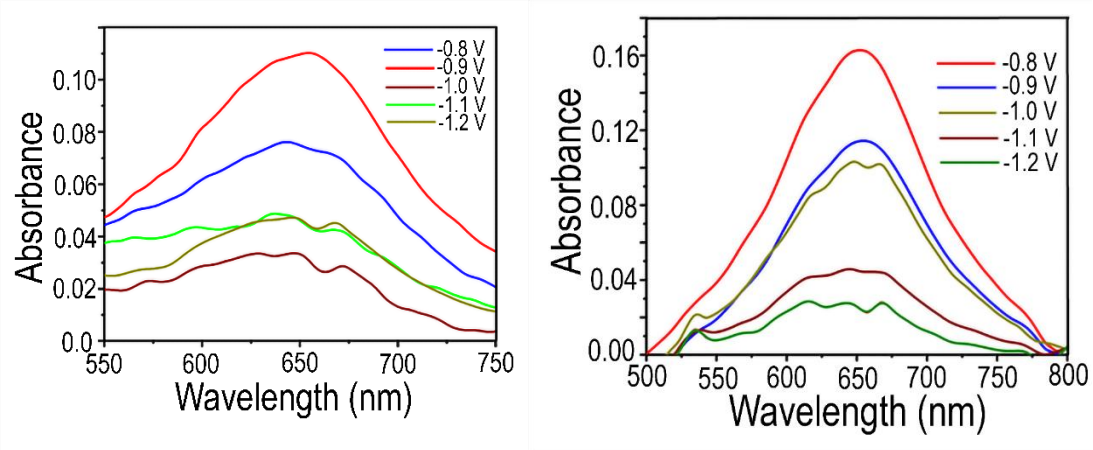

Fig. S15 A comparison of UV-visible absorption spectra of the graphene-supported Au_2Ag_2 (Left) and Au_4Cu_2 (Right) NCs for ENRR at different potentials after 2 hours incubation using indophenol assay.

Table S1 Crystallographic data for the Au_4Cu_2, Au_2Ag_2 Nanoclusters and Au complex.

	In this Work	**In this Work**	**In this Work**
Empirical formula	$C_{84}H_{60}Au_4Cu_2P_2$	$C_{68}H_{50}Ag_2Au_2P_2$	$3(C_{26}H_{20}AuP)\cdot CH_2Cl_2$
Formula weight	2046.20	1538.69	1765.99
Temperature (K)	170.00(10)	110.01(10)	170.00(10)
Crystal system	triclinic	monoclinic	monoclinic
Space group	P-1	$P2_1/n$	$P2_1/n$
a (Å)	12.6398(6)	11.3993(2)	13.1746(8)
b (Å)	16.7456(9)	21.6280(3)	12.7141(8)
c (Å)	18.5200(9)	21.9620(3)	39.686(4)
α (deg)	88.962(4)	90	90
β (deg)	76.498(4)	93.7590(10)	94.670(7)
γ (deg)	69.963(4)	90	90
Volume ($Å^3$)	3572.7(3)	5402.95(14)	6625.5(9)
Z	2	4	4
ρ_{calc} (g/cm^3)	1.902	1.892	1.770
μ (mm^{-1})	8.855	6.230	6.824
F(000)	1936.0	2960.0	3408.0
Crystal size (mm^3)	0.26 × 0.08 × 0.03	0.23 × 0.21 × 0.11	0.02 × 0.01 × 0.01
2Θ range for data collection (deg)	3.534 to 62.068	3.766 to 62.042	3.346 to 62.188
Index ranges	-18 ≤ h ≤ 17, -23 ≤ k ≤ 22, -20 ≤ l ≤ 26	-14 ≤ h ≤ 14, -25 ≤ k ≤ 29, -21 ≤ l ≤ 31	-18 ≤ h ≤ 14, -18 ≤ k ≤ 14, -56 ≤ l ≤ 55
Reflections collected	59738	45818	49079
Independent reflections	19237 [R_{int} = 0.0594, R_{sigma} = 0.0724]	14759 [R_{int} = 0.0235, R_{sigma} = 0.0271]	17752 [R_{int} = 0.1156, R_{sigma} = 0.1321]
Data / restraints / parameters	19237/127/829	14759/0/667	17752/474/784
Goodness-of-fit on F^2	1.056	1.027	1.095
Final R indexes [I>=2σ (I)]	R_1 = 0.0517, wR_2 = 0.1200	R_1 = 0.0259, wR_2 = 0.0598	R_1 = 0.1560, wR_2 = 0.3465
Final R indexes [all data]	R_1 = 0.0851, wR_2 = 0.1306	R_1 = 0.0310, wR_2 = 0.0612	R_1 = 0.2070, wR_2 = 0.3686
Largest diff. peak/hole (e $Å^{-3}$)	5.66/-1.91	1.33/-1.84	5.54/-7.31

Table S2 A comparison of NRR performance of graphene-supported Au_4Cu_2 NCs with other reported electrocatalysts

Catalyst	Electrolyte	NH_3 yield	FE(%)	Reference
Au_4Cu_2/G NCs	**0.1 M KOH**	**4.14 μg·h^{-1}cm^{-2}**	**49.60**	**This work**
Cu_6/GO NCs	0.1 M KOH	4.8 μg·h^{-1}cm^{-2}	30.39	Ref.[3]
Bi/carbon black	pH 3.5, 1.0 M K^+	200 mmol NH_3 g^{-1} h^{-1}	66	Ref.[4]
Cu NPs on Ti_3C_2	0.1 M KOH	3.04 μmol·h^{-1}cm^{-2}	7.31	Ref.[5]
TiO_2-rGO	0.1 M Na_2SO_4	15.13 μg·h^{-1}mg$^{-1}_{cat.}$	3.3	Ref.[6]
Ru@ZrO_2/NC	0.01 M HCl	3.665 mgNH_3 h^{-1}mg $_{Ru}^{-1}$	21	Ref.[7]
Ru NPs	0.01 M HCl	21.4 mg h^{-1} m^{-2}	5.4	Ref.[8]
Ru SAs/N-C	0.05 M H_2SO_4	120.9 μg h^{-1} mg$^{-1}_{cat.}$	29.6	Ref.[9]
AuHNCs/ITO	0.5 M $LiClO_4$	3.9 μg cm^{-2} h^{-1}	30.2	Ref.[10]
Au nanorods	0.1 M KOH	1.6 μg·h^{-1}cm^{-2}	3.88	Ref.[11]
β-FeOOH nanorod	0.5 M $LiClO_4$	23.32 μg·h^{-1}mg$^{-1}_{cat.}$	6.7	Ref.[12]
Au/CeOx	0.1 M HCl	37.3 μmol h^{-1} mg$_{Au}^{-1}$	10.1	Ref.[13]
TiO_2 nanosheets	0.1 M Na_2SO_4	5.6 μg·h^{-1}cm^{-2}	2.5	Ref.[14]
Ru−O−V *pyramid* electron bridge	0.1 M Na_2SO_4	115 μg·h^{-1}mg$^{-1}_{cat.}$	51.48	Ref.[15]
B-TiO_2	0.1 M Na_2SO_4	14.4 μg·h^{-1}mg$^{-1}_{cat.}$	3.4	Ref.[16]
Nitrogen oxidation, facilitated by OH·	0.1 M K_2SO_4	8.3 nmol s^{-1} cm^{-2}	25.6	Ref.[17]
CoO/CuO-NA/CF	0.5 M NaOH	296.9 μmol·h^{-1}cm^{-2}	92.9	Ref.[18]
MoS_2/CC	0.1 M Na_2SO_4	4.94 μg·h^{-1}cm^{-2}	1.17	Ref.[19]
Mo SA/BN	0.1 M KOH	37.67 μg·h^{-1}mg$^{-1}_{cat.}$	13.27	Ref.[20]
Cu SA/N-doped carbon	0.1 M KOH	53.3 μg·h^{-1}mg$^{-1}_{cat.}$	11.7	Ref.[21]
MoSAs Mo_2C/NCNTs	0.1 M KOH	16.1 μg. h^{-1} μg$^{-1}_{cat.}$	7.1	Ref.[20]
1T-MoS_2/g-C_3N_4	0.1 M KOH	29.97 μg. h^{-1} μg$^{-1}_{cat.}$	20.48	Ref.[22]
FeSA-NO-C	0.1 M KOH	31.9 μg. h^{-1} μg$^{-1}_{cat.}$	11.8	Ref.[23]

References

1. G. W. Watt and J. D. Chrisp, *Anal. Chem.*, 1952, **24**, 2006−2008.
2. M. J. Frisch, G. W. Trucks, H. B. Schlegel, G. E. Scuseria, M. A. Robb, J. R. Cheeseman, G. Scalmani, V. Barone, G. A. Petersson, H. Nakatsuji, X. Li, M. Caricato, A. V. Marenich, J. Bloino, B. G. Janesko, R. Gomperts, B. Mennucci, H. P. Hratchian, J. V. Ortiz, A. F. Izmaylov, J. L. Sonnenberg, Williams, F. Ding, F. Lipparini, F. Egidi, J. Goings, B. Peng, A. Petrone, T. Henderson, D. Ranasinghe, V. G. Zakrzewski, J. Gao, N. Rega, G. Zheng, W. Liang, M. Hada, M. Ehara, K. Toyota, R. Fukuda, J. Hasegawa, M. Ishida, T. Nakajima, Y. Honda, O. Kitao, H. Nakai, T. Vreven, K. Throssell, J. A. Montgomery Jr., J. E. Peralta, F. Ogliaro, M. J. Bearpark, J. J. Heyd, E. N. Brothers, K. N. Kudin, V. N. Staroverov, T. A. Keith, R. Kobayashi, J. Normand, K. Raghavachari, A. P. Rendell, J. C. Burant, S. S. Iyengar, J. Tomasi, M. Cossi, J. M. Millam, M. Klene, C. Adamo, R. Cammi, J. W. Ochterski, R. L. Martin, K. Morokuma, O.

Farkas, J. B. Foresman and D. J. Fox, *Journal*, 2016.
3. A. Shehzad, C. Cui, R. Cheng and Z. Luo, *Nanoscale*, 2024, **16**, 14441−14447.
4. Y.-C. Hao, Y. Guo, L.-W. Chen, M. Shu, X.-Y. Wang, T.-A. Bu, W.-Y. Gao, N. Zhang, X. Su, X. Feng, J.-W. Zhou, B. Wang, C.-W. Hu, A.-X. Yin, R. Si, Y.-W. Zhang and C.-H. Yan, *Nat. Catal.*, 2019, **2**, 448−456.
5. A. Liu, X. Liang, Q. Yang, X. Ren, M. Gao, Y. Yang and T. Ma, *ChemPlusChem*, 2021, **86**, 166–170.
6. X. Zhang, Q. Liu, X. Shi, A. M. Asiri, Y. Luo, X. Sun and T. Li, *J. Mater. Chem. A*, 2018, **6**, 17303–17306.
7. H. C. Tao, C. Choi, L. X. Ding, Z. Jiang, Z. S. Hang, M. W. Jia, Q. Fan, Y. N. Gao, H. H. Wang, A. W. Robertson, S. Hong, Y. S. Jung, S. Z. Liu and Z. Y. Sun, *Chem*, 2019, **5**, 204−214.
8. D. Wang, L. M. Azofra, M. Harb, L. Cavallo, X. Zhang, B. H. R. Suryanto and D. R. MacFarlane, *ChemSusChem*, 2018, **11**, 3416–3422.
9. Z. Geng, Y. Liu, X. Kong, P. Li, K. Li, Z. Liu, J. Du, M. Shu, R. Si and J. Zeng, *Adv. Mater.*, 2018, **30**, 1803498.
10. M. Nazemi, S. R. Panikkanvalappil and M. A. El-Sayed, *Nano Energy*, 2018, **49**, 316−323.
11. D. Bao, Q. Zhang, F.-L. Meng, H.-X. Zhong, M.-M. Shi, Y. Zhang, J.-M. Yan, Q. Jiang and X.-B. Zhang, *Adv. Mater. (Weinheim, Ger.)*, 2017, **29**, 1604799.
12. X. Zhu, Z. Liu, Q. Liu, Y. Luo, X. Shi, A. M. Asiri, Y. Wu and X. Sun, *Chem. Commun.*, 2018, **54**, 11332–11335.
13. S.-J. Li, D. Bao, M.-M. Shi, B.-R. Wulan, J.-M. Yan and Q. Jiang, *Adv. Mater. (Weinheim, Ger.)*, 2017, **29**, 1700001.
14. R. Zhang, X. Ren, X. Shi, F. Xie, B. Zheng, X. Guo and X. Sun, *ACS Appl. Mater. Interfaces*, 2018, **10**, 28251−28255.
15. Y. Sun, X. Li, Z. Wang, L. Jiang, B. Mei, W. Fan, J. Wang, J. Zhu and J.-M. Lee, *J. Am. Chem. Soc.*, 2024, **146**, 7752–7762.
16. Y. Wang, K. Jia, Q. Pan, Y. Xu, Q. Liu, G. Cui, X. Guo and X. Sun, *ACS Sustain. Chem. Eng.*, 2019, **7**, 117−122.
17. K. Dong, Y. Yao, H. Li, H. Li, S. Sun, X. He, Y. Wang, Y. Luo, D. Zheng, Q. Liu, Q. Li, D. Ma, X. Sun and B. Tang, *Nat. Synth.*, 2024, **3**, 763–773.
18. S. Chen, G. Qi, R. Yin, Q. Liu, L. Feng, X. Feng, G. Hu, J. Luo, X. Liu and W. Liu, *Nanoscale*, 2023, **15**, 19577−19585.
19. L. Zhang, X. Ji, X. Ren, Y. Ma, X. Shi, Z. Tian, A. M. Asiri, L. Chen, B. Tang and X. Sun, *Adv. Mater.*, 2018, **30**, e1800191.
20. L. Shi, S. Bi, Y. Qi, R. He, K. Ren, L. Zheng, J. Wang, G. Ning and J. Ye, *ACS Catal.*, 2022, **12**, 7655−77663.
21. W. Zang, T. Yang, H. Zou, S. Xi, H. Zhang, X. Liu, Z. Kou, Y. Du, Y. P. Feng, L. Shen, L. Duan, J. Wang and S. J. Pennycook, *ACS Catal.*, 2019, **9**, 10166–10173.
22. X. Xu, X. Tian, B. Sun, Z. Liang, H. Cui, J. Tian and M. Shao, *Appl. Catal. B- Environ.*, 2020, **272**, 118984.
23. Y. Li, J. Li, J. Huang, J. Chen, Y. Kong, B. Yang, Z. Li, L. Lei, G. Chai, Z. Wen, L. Dai and Y. Hou, *Angew. Chem. Int. Ed.*, 2021, **60**, 9078–9085.